City Research Online

City St George's, University of London

Citation: Zifan, A., Liatsis, P. & Chapman, B. E. (2013). The use of the Kalman filter in the automated segmentation of EIT lung images. Physiological Measurement, 34(6), pp. 671-694. doi: 10.1088/0967-3334/34/6/671

This is the accepted version of the paper.

This version of the publication may differ from the final published version. To cite this item please consult the publisher's version.

Permanent repository link: https://openaccess.city.ac.uk/id/eprint/7740/

Link to published version: https://doi.org/10.1088/0967-3334/34/6/671

Copyright and Reuse: Copyright and Moral Rights remain with the author(s) and/or copyright holders. Copies of full items can be used for personal research or study, educational, or not-for-profit purposes without prior permission or charge, unless otherwise indicated, provided that the authors, title and full bibliographic details are credited, a hyperlink and/or URL is given for the original metadata page and the content is not changed in any way. For full details of reuse please refer to City Research Online policy.

City Research Online: http://openaccess.city.ac.uk/ publications@citystgeorges.ac.uk

The use of the Kalman Filter in the automated segmentation of EIT lung images

A Zifan, [1] **P Liatsis,** [2] **B E Chapman** [1]

[1] Division of Biomedical Informatics
University of California, San Diego (UCSD), USA

[2] Department of Electrical and Electronic Engineering
City University, Northampton Square, London, UK

E-mail: azifan@ucsd.edu

Abstract
In this paper, we present a new pipeline for the fast and accurate segmentation of impedance images of the lungs using Electrical Impedance Tomography (EIT). EIT is an emerging, promising, non-invasive imaging modality that produces real-time, low spatial but high temporal resolution images of impedance inside a body. Recovering impedance itself constitutes a non-linear ill-posed inverse problem, therefore the problem is usually linearized, which produces impedance-change images, rather than static impedance ones. Such images are highly blurry and fuzzy along object boundaries. We provide a mathematical reasoning behind the high suitability of the Kalman filter when it comes to segmenting and tracking conductivity changes in EIT lung images. Next, we use a two-fold approach to tackle the segmentation problem. First, we construct a global lung shape to restrict the search region of the Kalman filter. Next, we proceed with augmenting the Kalman filter by incorporating an adaptive foreground detection system to provide the boundary contours for the Kalman filter to carry out the tracking of the conductivity changes as the lungs undergo deformation in a respiratory cycle. The proposed method has been validated by using misclassified area, false positive rate, and compared to previous methods. The results show the proposed automatic method can be a fast and reliable segmentation tool for EIT imaging.

Keywords: EIT; ill-posed problems; impedance; regularization; segmentation; Kalman filter.

1. Introduction

There is evidence that the electrical properties of tissue vary according to its state of health (Pethig, 1984), which raises the possibility of distinguishing between healthy and abnormal tissue, once these electrical properties are known. Hence, if this latent conductivity distribution among different tissues could somehow be computed from measurements, a powerful diagnostic tool could be developed. Although the

problem of conductivity distribution reconstruction from surface measurements is non-linear and ill-conditioned, it can be solved using 2D or 3D finite element methods (FEMs) subject to using appropriate regularization strategies (Molinari, 2003) and (Holder, 2005).

Electrical impedance tomography (EIT) forms images of the interior of the human body based on the passive electrical properties (i.e., electric conductivity and permittivity) of the organs inside the body. EIT is very useful in monitoring patient lung volume changes, due to the large conductivity contrast of air compared to other tissues in the thorax. The large change in lung impedance with respiration, and the ease of use of impedance tomography, as a monitoring technique, has led to a significant body of research in lung impedance imaging (Frerichs, 1998, 1999, 2000, 2002, and 2009; Hahn et al. 1996; Victorino et al. 2004; Grychtol et al. 2010). However, the spatial resolution of EIT images is very low and this makes it hard to determine the outline of these rapidly changing regions during a breathing cycle. In comparison to magnetic resonance imaging (MRI) and computed tomography (CT), EIT suffers from poor spatial resolution due to noise, low sensitivity of boundary voltages to inner conductivity perturbations and a limited number of boundary voltage measurements.

X-ray computed tomography (CT) imaging generates 2D sections of the body, which are approximately 1*mm* in thickness (Hendee and Russell, 2002). Moreover, sub-millimeter spatial resolution having accurate discrimination between tissues (better than 1% attenuation change) can be achieved. This is not the case in EIT, where the spatial resolution is quite low (in the order of 10-20% of the object dimension)(Holder, 2005). Although, it should be noted that the poor spatial resolution of EIT does not come as a surprise, when one is reminded of the nature of the EIT image reconstruction problem itself (i.e., inverse, nonlinear and ill-posed). The latter factors impede accurate estimation of the internal structure boundaries. Moreover, the spatial resolution of the EIT images reduces even further with the rasterisation process, where FEM model results are mapped onto a rectangular grid for further image processing. This rasterisation step introduces further fuzziness in the reconstructed regions of conductivity changes in the EIT images of the lungs, and makes it even harder to determine the outlines of these dynamic regions during the breathing cycle. A visual comparison of an EIT image and its CT counterpart for imaging of the thorax is shown in figure 1.

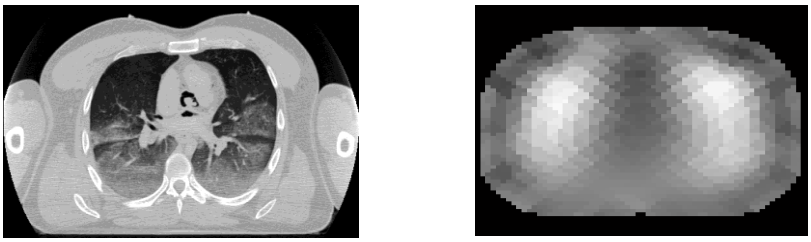

(a) (b)

Figure 1: Spatial resolution**:** (a) A typical cross-sectional CT image of the thorax, (b) EIT difference image (brighter regions correspond to larger conductivity changes).

The problem of medical image segmentation is a major obstacle in medical imaging (Pham et al., 200l ; Zhang, 2001; Singh 2010; Prasantha et al., 2010). The goal is to simplify the representation of an image,

by partitioning the medical image into multiple segments, such as locating organ boundaries, or abnormal growth of body tissue such as tumors. Typically a digital image represents medical images in their raw form, with pixel values indicating relevant physical quantity values that allow distinction between different types of body tissue contrast. Segmentation is an arduous task due to the presence of noise, organ motion, cluttered objects, occlusion, heterogeneous texture, and many other factors. A common problem encountered in practice is the lack of sufficient contrast between object boundaries in medical images. To address this problem, several segmentation approaches have been proposed in the literature, with many of them providing rather promising results (Ma et a., 2010; Daniel et al, 2008).

As discussed previously, the segmentation process, is extra difficult in EIT due the ill-posedness of the reconstruction problem, which lends itself into images with fuzzy organ boundaries. Hence, the common approach of segmenting EIT lung images is to manually define a region of interest (Frerichs, 1998, 1999, 2000, 2002, Grychtol, 2010), and derive statistical measures. A manual segmentation approach is not desirable, firstly because it involves user interaction (which could be laborious and subject to errors), and secondly because if the goal of EIT is to be used as a bedside monitoring tool, a systematic approach should be developed that brings user interaction to a minimum.

A fast segmentation method using a spatio-temporal segmentation framework was introduced in (Zifan et al, 2011). In the former method, in the first step, after impedance change images are reconstructed, segmentation is carried out directly on the finite element (FE) meshes prior to any rasterisation onto a regular grid. This prevents regions from becoming even fuzzier due to interpolation, and facilitates the estimation of accurate measurement results, which is a prerequisite for the extraction of much needed ventilation parameters from EIT images. In the second step, the authors use a probabilistic model, which accommodates for both temporal and spatial contiguity of mesh element values in order to segment and extract regions of conductivity changes directly from the EIT lung FE meshes.

In this paper, we present an alternative fast and robust segmentation framework that incorporates a search-space constrained Kalman filter, via anatomical information provided by a statistical shape model of the lung lobes and the thoracic wall, coupled with an automatic foreground detector in order to track conductivity changes in the lungs as they go through deformation in a respiratory cycle. Section 2 provides a brief background of EIT, the Kalman filter and the relationship between L^2 -norm regularization reconstructions and the Kalman filter. In Section 3, the segmentation pipeline is introduced, which discusses a framework for generating a statistical lung shape model and an adaptive foreground detection algorithm to enhance Kalman filtering in segmenting EIT lung images. Section 4 provides the simulation results. Finally, we conclude the paper in Section 5.

2. Background

In this section, we provide a brief background of EIT and the Kalman filter, which will be used later on in the simulation experiments. Moreover, we discuss the reasons behind the suitability of the Kalman filter when it comes to segmenting EIT images.

2.1. Electrical Impedance tomography

In EIT, typically low amplitude current is injected through a single (or multiple) ring of electrodes attached around the medium under study. Current is injected into one electrode pair and the voltages between other electrodes are recorded. The injection is then successively shifted so that all electrode pairs

are examined using either a single frequency (50 kHz) or a range of frequencies (up to 1 MHz). In order to reconstruct images of tissue conductivity, the following two problems must be solved: the forward problem and the inverse problem. The forward problem is the determination of the voltage distribution for a known conductivity distribution in the imaged domain, while the inverse problem consists of conductivity image reconstruction using the measured voltages at the surface of the medium. This is shown schematically in figure 2 for an adjacent current injecting protocol, where actual measurements taken from the body are combined with the voltages obtained from a mathematical model in order to obtain the reconstructed conductivity image.

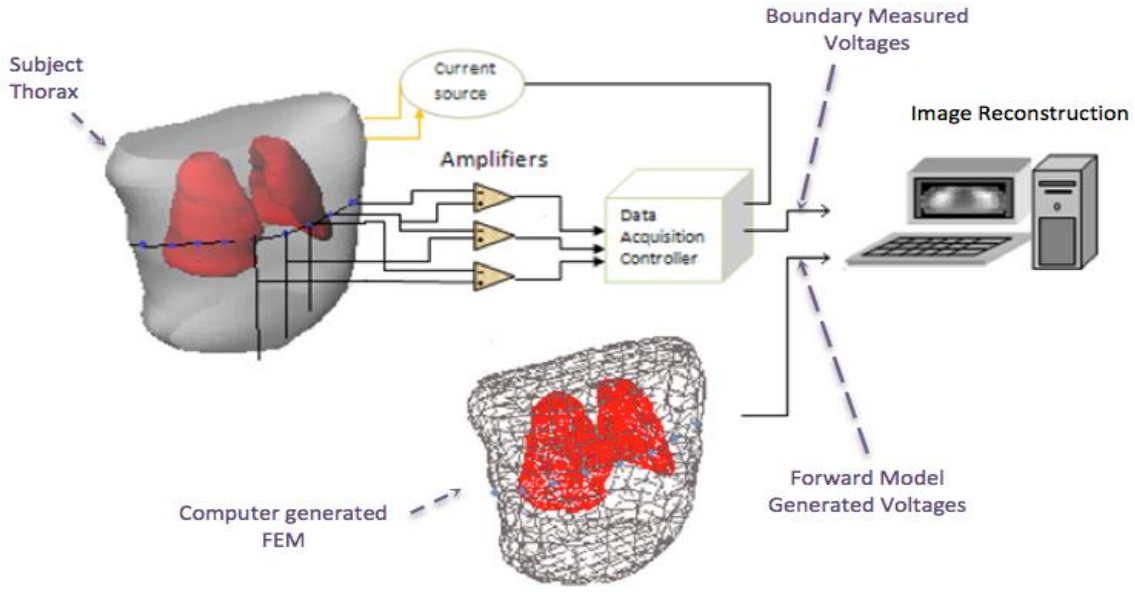

Figure 2: EIT imaging system: Rotating current injection (I) is performed between pairs of adjacent surface electrodes on a cross-section of the human thorax, and the resulting voltages (V) are measured between other pairs of electrodes

2.1.1. Forward problem

The governing equation for the voltage field produced by applying current across a domain Ω is,

$$\nabla \cdot (\sigma + \omega\varepsilon)\nabla\varphi = 0, \tag{1}$$

which is an elliptical partial differential equation, where σ is the conductivity of the medium, φ is the electric potential, ω is the frequency, and ε is the electric permittivity (Holder, 1993). Equation (1) is reduced to the standard governing equation for EIT, $\nabla \cdot (\sigma\nabla\varphi) = 0$, when the angular frequency is sufficiently low or direct current is used. By using an excitation signal and permittivity distribution we can estimate the induced electrical measurements at the electrodes, using equation (1) under appropriate Dirichlet or Neumann boundary conditions (Holder, 1993). This is often referred to as the forward problem. If I_l is the current injected to the *l-th* electrode E_l, which has a contact impedance z_l, the

complete electrode boundary conditions (Cheng et al., 1989) are:

$$V_l = \varphi + z_l \sigma \frac{\partial \varphi}{\partial n} \tag{2}$$

$$I_l = \int_{E_l} \sigma \frac{\partial \varphi}{\partial n} dS \tag{3}$$

where V_l is the constant voltage on electrode E_l, n the outward unit normal vector and,

$$\sigma \frac{\partial \varphi}{\partial n} = 0 \tag{4}$$

is the current density on the boundary inter-electrode gap. Finally, the solution of equation (1) can be approximated using the method of weighted residuals using Galerkin test functions to arrive at the following formula (Holder, 1993),

$$\int_\Omega \sigma \nabla \varphi \cdot \nabla \vartheta dV = \sum_{l=1}^{L} \int_{E_L} \frac{1}{z_l} (V_l - \varphi) \vartheta dS \tag{5}$$

where ϑ is the test function. Equation (5) can then be discretized and solved using finite elements using linear or quadratic elements of different orders taking the form,

$$\begin{bmatrix} A_M & A_W \\ {A_W}^T & A_P \end{bmatrix} \begin{bmatrix} \Phi \\ V \end{bmatrix} = \begin{bmatrix} 0 \\ I \end{bmatrix} \tag{6}$$

where I is the current pattern applied to the ring of electrodes, and $\Phi = (\varphi_1, \dots, \varphi_n)$ represents the discrete approximation of the potential. Using the same test functions to approximate potentials, $\vartheta = \sum_{i=0}^{N} \vartheta_i w_i$, the entries of the A matrix structure of Equation (6) can be obtained as follows,

$$\begin{aligned} A_{M,ij} &= \int_\Omega \sigma \nabla w_i \cdot \nabla w_j dV + \sum_{l=1}^{L} \int_{E_L} \frac{1}{z_l} (w)_i w_j dS, \\ A_{W,ij} &= -\int_{E_L} \frac{1}{z_l} w_i dS \ , \\ A_p &= diag(|E_l| z_l^{-1}) \end{aligned} \tag{7}$$

where $i, j = 1, \dots, n$ is the number of vertices, and L is the number of electrodes. The A matrix in (6) is sparse, symmetric (in the case of complex conductivities and contact impedances, this means that the real and imaginary parts are symmetric), and the real part is positive definite.

2.1.2. Inverse problem

If we represent the forward operator g by $g(m)=d$, where m is the model and d is the boundary measurement voltage vector, as the goal is to come up with a model that yields the actual measured voltages d_T, the simplest approach is to minimize the following sum, which is the minimum of the sum of square errors,

$$\|d_T - g(m)\|_F^2 \tag{8}$$

where F denotes the Frobenius norm. Now, assuming no model null-space and that only the data misfit term as described in (8) is required to solve the inverse problem, if we could somehow linearize the g operator, we could use linear methods such as the conjugate gradient (CG) to derive the critical points of (8). This can be done, by linearizing the forward problem in the neighborhood of a reference model m_0, using a Taylor expansion,

$$\begin{aligned} g(m) &= g(m_0) + \left.\frac{\partial g}{\partial m}\right|_{m=m_0}(m-m_0) + \left.\frac{\partial^2 g}{\partial m^2}\right|_{m=m_0}(m-m_0)^2 + \cdots \\ &\approx g(m_0) + \nabla g(m_0)(m-m_0) + \cdots \end{aligned} \tag{9}$$

Ignoring higher order terms,

$$g(m) = g(m_0) + G(m-m_0) \tag{10}$$

where, G is a rectangular matrix that gives the sensitivity of the forward problem to the model parameters at $m = m_0$,

$$G_{ij} = \left.\frac{\partial g_j}{\partial m_i}\right|_{m=m_0} \tag{11}$$

Next, we use this Taylor expansion to linearize the inverse problem,

$$d = g(m) \approx g(m_0) + G(m-m_0) \tag{12}$$

Let, $\delta d = d - g(m_0); \delta m = m - m_0$ denote the perturbation, so:

$$\delta d = G\delta m \tag{13}$$

which is the linearized inverse problem for the perturbation of m about $m = m_0$.

As the problem is ill-posed (small errors in the measurements may introduce large errors in the reconstruction) the minimization of the voltage error in (8), is not likely to yield good results. This is because in practice linear least squares calculations usually involve singular matrices or matrices that are numerically singular (small eigenvalues). For a unique solution, we must add some additional information regarding the conductivity that is independent of the data known as the prior. Regularization mitigates

these singularities. This can be done either by discarding small eigenvalues or by penalizing the size of the solution as well as the data misfit. In other words, the minimization problem of (8) can be written as,

$$\min(\|\delta d_T - G(\delta m)\|^2 + \|\delta m\|^2) \tag{14}$$

The first term of (14) is the data misfit, and the second term is referred to as the regularization term. We can also introduce a factor λ that controls the tradeoff between the two terms and not only consider the possibility of minimizing the norm itself, but the norm of some linear function of the form,

$$\min(\|\delta d_T - G(\delta m)\|^2 + \lambda\|R\delta m\|^2) \tag{15}$$

where $R \equiv \partial^n, n = 0,1,2,\ldots$ and ∂^n is an *n*-th order discrete difference operator. In this case, the second term in (15) penalizes the slope, roughness, or higher order derivatives of the model. This is useful when one seeks a smooth solution.

Methods incorporating the L^2-norm as the regularization term, as in (14) or (15), are called Tikhonov regularization (Tychonoff and Arsenin, 1977) in Inverse theory and Ridge regression (Hoerl, 1962) in Statistics. The use of this particular norm, as explained in Section 2.3, provides the key reasoning behind why the Kalman filter is useful for the segmentation/tracking of objects in image sequences obtained from the solution of ill-posed inverse problems that use the L^2-norm as the regularization term.

2.2. Kalman filter

The Kalman filter (Anderson and Moore, 1979) is a set of linear equations that provides an efficient, recursive means to estimate the state of a process in such a way that minimizes the mean of the squared error. The filter supports estimations of past, present, and future states of a system, even when the precise nature of the modeled system is unknown. It assumes that the posterior density is Gaussian at every time step, and that the current state x_k and observation z_k are linearly dependent on the past state x_{k-1}. The linear system of equations is as follows:

$$x_k = Ax_{k-1} + w_{k-1} \tag{16}$$

$$z_{k-1} = Hx_{k-1} + v_{k-1} \tag{17}$$

where $\{w_k\}$ is the process white Gaussian noise with zero mean and covariance $Q_k \geq 0$ *(*$w_k \sim N(0, Q_k)$*)*, $\{v_k\}$ is the measurement white Gaussian noise with zero mean and covariance $R_k > 0$. The covariance matrices Q_k and R_k are assumed to be statistically independent. The matrix *A* is considered known and relates the former state x_{k-1} to the current state x_k. The matrix *H* is also known and relates the state x_k to the observation z_k. We define $\hat{x}_k^- \in \mathcal{R}^n$ to be the *a priori* state estimate at step *k*, given knowledge of the process prior to step *k*, and $\hat{x}_k \in \mathcal{R}^n$ to be the a posteriori state estimate at step *k*, given measurements (Bucy and Joseph, 2005). Then, the a priori and a posteriori estimate error becomes (Anderson and Moore, 1979),

$$e_k^- = x_k - \hat{x}_k^- \, , e_k = x_k - \hat{x}_k \tag{18}$$

respectively. The a priori estimate error covariance is then,

$$P_k^- = E[e_k^- e_k^{-T}] \tag{19}$$

and the a posteriori estimate error covariance is,

$$P_k = E[e_k e_k{}^T] \tag{20}$$

In deriving the equations for the Kalman filter, the goal is to find the equations that compute the a posteriori state estimate $\hat{x}_k$ as a linear combination of an a priori estimate $\hat{x}_k^-$ and a weighted difference between an actual measurement and a measurement prediction $H\hat{x}_k^-$ as described in (21),

$$\hat{x}_k = \hat{x}_k^- + K(z_k - H\hat{x}_k^-) \tag{21}$$

The matrix *K* in (21) is the gain. One form of the resulting *K* that minimizes (21) is given by (Anderson and Moore, 1979),

$$K_k = P_k^- H^T (HP_k^- H^T + R)^{-1} \tag{22}$$

A Kalman filter uses a feedback control in order to estimate a process; it estimates the process state at some time *k* and then obtains feedback in the form of (noisy) measurements.

2.3. Choice of Regularization and the Kalman filter

It is not hard to see why the Kalman filter is a good choice when it comes to segmenting L^2-norm reconstructions. This can be done by re-examining (15) from a probabilistic point of view. Let us assume that we have a set of i.i.d. voltage measurements $d_{obs} = [d_1, \dots, d_G]$, where *G* is the total number of measurements. Our goal is find a model $\hat{\theta}$ which best fits the data. In other words a model, which is the maximum a posteriori estimator (MAP) (Sorenson, 1980) of θ,

$$\hat{\theta} = arxmax\big(p(\theta|V_{obs})\big) \tag{23}$$

Using Bayes rule,

$$p(\theta|V_{obs}) = \frac{p(V_{obs}|\theta)p(\theta)}{p(V_{obs})} \tag{24}$$

Hence,

$$\hat{\theta} = arxmax\left(\frac{p(V_{obs}|\theta)p(\theta)}{p(V_{obs})}\right) \approx arxmax\prod_{i=1}^{G} p(V_{obs_i}, \theta)p(\theta) \tag{25}$$

Now, if we assume our data comes from a multivariate Gaussian distribution $p(\theta) \sim N(\mu, \Sigma)$, which has zero mean $\mu = 0$ and a covariance of ${\sigma^2 I}/{\lambda}$, where σ is the variance, λ the regularization term, and I the identitiy matrix. Then $\hat{\theta}$ becomes,

$$\hat{\theta} = arxmax\prod_{i=1}^{G} \frac{\lambda}{2\pi\sigma^2} exp\left(\frac{-\left(\delta d_i - \theta^T(\delta m_i)\right)^2}{2\sigma^2}\right)... \tag{26}$$

$$exp\left(-\frac{\lambda\theta^T\theta}{2\sigma^2}\right)$$

Taking the logarithm of (26) results in the minimization problem of,

$$Q(\theta) = \sum_{i=1}^{G}\left(\delta d_T - \theta^T(\delta m)\right)^2 + \lambda\theta^T\theta \tag{27}$$

Comparing the second terms of (27) and (15) implies that $\lambda\theta^T\theta = \lambda\|R\delta m\|^2$. This means that by using an L^2 norm we impose a Gaussian prior assumption on the unknown parameter θ. This latter fact explains why the Kalman filter suits best as it also uses a Gaussian distribution on the data.

3. Methodology

The proposed method uses a symbiotic cooperation between a anatomically constrained Kalman filter and an adaptive foreground detector to track changes in lung conductivity (i.e., absolute conductivity value changes of the mesh elements corresponding to lung regions) in EIT lung images. However, the Kalman filter requires Region of Interest (ROI) as the initial boundary, in our case the lung contours, to be able to track any conductivity changes. Hence, in the first stage a framework is introduced to build an initial global lung model using realistic anatomical information of the lungs inside the thorax. This is achieved through building a 2D statistical shape model of the lungs and the thoracic wall obtained from 2D cross-sectional CT images of 50 subjects. Once such a shape model is built, it can be warped onto a new patient's thorax geometry in order to confine the search region to speed up calculations. Furthermore, an automatic foreground detector is introduced that not only extracts an initial boundary contour for the Kalman filter, but also acts as a means for penalizing and preventing the Kalman filter estimates from diverging from the true lung boundaries. Finally, in order to prove the efficacy of the method, the proposed method is tested against the statistical segmentation approach of (Zifan et al., 2011). A flow-chart of the proposed methodology is shown in figure 3.

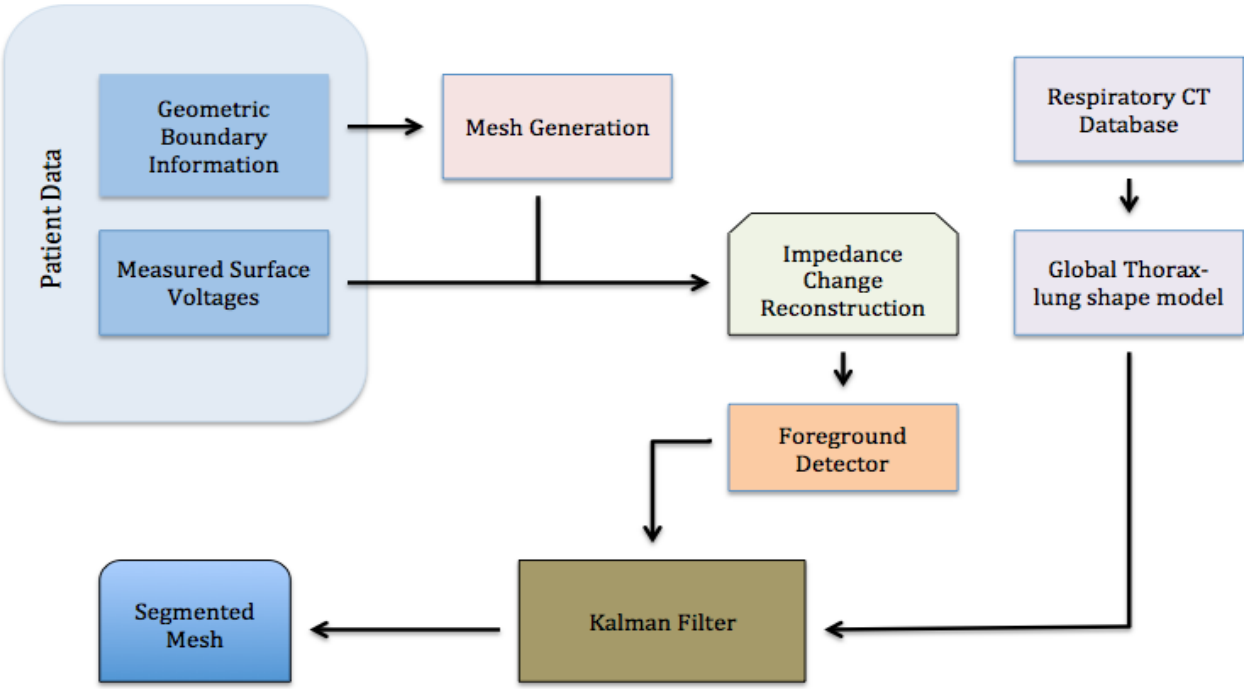

Figure 3. Flowchart descring the flow of the segmentation process pipeline.

As it can be seen from the above figure, a two-fold approach is used to tackle the EIT segmentation problem. First, a statistical lung-thorax shape model is built in order to restrict the search region of the Kalman filter. Second, for each new subject, using the surface voltage measurement, provided there exists geometric thoracic boundary information, a patient specific 2D mesh is generated via triangulation, and the inverse problem is solved on the former mesh (it should be noted that no Rasterisation is carried out to reduce boundary fuzziness due to subsequent grid interpolation). Finally, we proceed with augmenting the Kalman filter by incorporating an adaptive foreground detection system, which will feed its resulting change detection region information, in order to provide the boundary contours for the initialization and subsequent processing of the Kalman filter to carry out the tracking of the conductivity changes as the lungs undergo deformation in a respiratory cycle.

3.1 Global Lung-thorax Shape Model: Delineating the Lungs and Thoracic Wall

In order to derive a global shape model for the lungs and thoracic wall, which would explain the population mean shape and the variation within the subjects, we use Statistical shape modeling (SSM). Statistical shape models are commonly used in medical image analysis, computational anatomy, and computer vision in order to model the shape variability of biological organs (Fleute and Lavallee, 1998; Subsol et al, 1998; Rajamani et al, 2007, Dam et al. 2008). When it comes to building statistical models, one requires a set of segmentations of the organ of interest, as well as a set of landmarks, which are defined over the set of shapes in the training set. One major task, is finding correspondences between

points of different shapes, which is time-consuming and tedious. Given every image in the training set, we proceed with the following three major steps:

1. Segmentation of the structure of interest (i.e., lungs and thoracic wall) from the data set
2. Multi-resolution non-rigid registration
3. Automatic Landmarking and Statistical shape Model Generation

In brief, given the cross-sections of the 50 CT volume images, the anatomical structures of interest from each CT image are extracted. Next, a dense non-rigid image deformation is carried out to register all images into one global one. Next, the final mean shape image (consisting of the thoracic wall and lung lobe locations) is meshed, in order to create landmarks on the desired object boundaries. Principal component analysis (PCA) is applied next not only to reduce the dimensionality of the data and, but to build the final shape model describing the variance of shapes within the dataset. In what follows, each step is discussed in detail.

3.1.1. Segmentation

In order to build the atlas, cross-sectional slices of the thorax at the lower thorax level (4^{th}-6^{th} intercostal space on the mid-clavicular line) of 50 subjects were obtained from the ELCAP Public Lung Image Database in order to build the anatomical data set. The lung dataset consists of 50 CT scans obtained in a single breath hold with a 1.25 mm slice thickness.

(a) (b)

Figure 4. Extracting the lungs and the thoracic boundary of a sample cross-sectional CT : (Left) Original CT cross-section, (Right) Segmented image.

In order to build the shape model, the lungs and the thorax boundary are automatically extracted. For each CT slice, the slice is thresholded using the algorithm proposed in (Hoffman, and Reinhardt, 2001) as follows: Let T_i be the threshold value at step *I* and μ_1, μ_2 be the average intensities of the body pixels and non-body pixels, respectively. Then, the threshold for step *I + 1* is set to the mean of μ_1, μ_2. This iterative threshold update procedure is repeated until there is no change in the threshold, i.e. $T_{i+1} = T_i$. In order to extract the thoracic wall, the image is inverted; the holes are filled using region filling. In order to segment out the lung lobes, the background is removed using the method from (Hoffman, and Reinhardt, 2001). The final segmentation is shown in figure 4(b).

3.1.2. Registration

The problem of the registration of two images can be described as finding an optimal transformation T^*, which can match a transformed reference image to a target image. The transformation T itself, constitutes a spatial mapping which relates the positions of features in one image with the corresponding features of the other image. Overall, the optimal transformation T^* is calculated by minimizing a cost function Q,

$$T^* = argmin\{Q(T)\} = argmin\{Q_{sim}(\ I_{mov},\ I_0 \circ T) + Q_{reg}(T)\}, \qquad T \in \Gamma \tag{28}$$

where I_0 and I_{mov} denote the reference image and the target image, respectively. The set Γ, is the set of admissable transfromations. Q_{sim}, denotes the similairty measure, and Q_{reg} is the regulariztion term wich penalizes undesired tranformation.

In order to construct the similiaty measure, different features can be used. A simple measure, is the sum of squared differences (SSD) (Modersitzki, 2004), which translate to the following formulation, using SSD as a metric,

$$Q_{sim}(\ I_{mov},\ I_0 \circ T) = Q_{SSD}(\ I_{mov},\ I_0 \circ T) = \frac{1}{2}\|\ I_{mov} -\ I_0 \circ T\|^2 \tag{29}$$

The SSD metric forms the basis of most inensity-based image registration algorithms and one can use classical optimization methods in order to find the optimal solution. However, optimizing Equation (29) over the space of non-parametric transformations leads to unstable solutions. Therefore, the added regularisation term Q_{reg}, overcomes this problem,

$$Q_{reg}(T) = \xi\|\nabla T\|^2 \tag{30}$$

where ξ controls the amount of regularisation. Thus, the cost function can be re-written as:

$$\begin{aligned} Q = Q_{sim}(\ I_{mov},\ I_0 \circ T) + Q_{reg}(T) &= Q_{SSD}(\ I_{mov},\ I_0 \circ T) + Q_{reg}(T) \\ &= \frac{1}{2}\|\ I_{mov} -\ I_0 \circ T\|^2 + \xi\|\nabla T\|^2 \end{aligned} \tag{31}$$

Solving Equation (31), is computationally expensive. A simple, yet intuitive method was proposed by Thirion (Thirion, 1995), namely Demons, and its variants (Cachier and Bardinet, 2003; Wang and Dong, 2005; Rogeli and Kovacic, 2006), tackling non rigid registration as a diffusion process problem, We employ Demons' multiresolution non-rigid registration method, to find the correspondences between matched labeled shapes (i.e., thoracic walls and lobes) rather than gray-level images, i.e., image segmentations where each voxel value indicates the type of structure this voxel belongs to. Given a fixed image $\mathrm{I_s}(\chi)$ with dimensions $L \times M$ and a moving image $\mathrm{I}_{mov}(\chi)$, the non-rigid image registration is treated as an optimization problem that aims at finding the displacement of each pixel denoted by the vector $D_s(\chi) = [d_s(0,0), \dots, d_s(l,m), \dots, d_s(L,M)]^T$, where $d_s(l,m) = [\Delta x, \Delta y]$ is the displacement vector field, so as to get a reasonable alignment of the images. The algorithm utilizes a diffusion model where the object boundaries in one image are characterized as semi-permeable membranes, and the other

image is allowed to diffuse through these membranes following the formulation of Ibanez (Ibanez et al, 2005),

$$D_s(\chi) \cdot \nabla \mathrm{I_s}(\chi) = -(I_{mov}(\chi) - \mathrm{I_s}(\chi)) \tag{32}$$

the displacement vector is denoted by $D_s(\chi)$, and the static image by $\mathrm{I_s}(\chi)$. Assuming intensity preservation, the image moving velocity *v* is computed. In general, *v* is considered to be a displacement vector field *u*=-*v* in image registration. Next, at each point *p* out of the *n* points on the image, the displacement vector becomes (Thirion, 1995),

$$u(p) = -\frac{(\,I_0 \cdot T(p) - \;I_{mov}(p))}{(\,I_0 \cdot T(p) - \;I_{mov}(p))^2 + \|\nabla\; I_{mov}(p)\|^2} \nabla\; I_{mov}(p) \tag{33}$$

In summary, the spatial transformation process is an iterative one. In what follows, we provide the main steps involved in the Demons method:

(a) Given the current transformation *T(n),* compute the displacement field *u(n).*
(b) Smooth the displacement field $u(n)$: $u(n) \leftarrow G_\sigma * u(n)$, where G_σ is a Gaussian smoothing filter.
(c) Compute the transformation $T(n+1) \leftarrow T(n) + u(n)$.

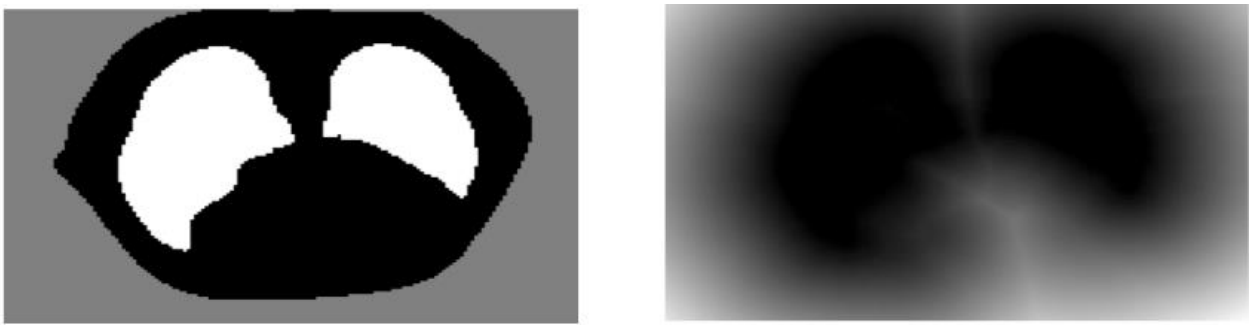

(a) (b)

Figure 5: Example of: (a) sample segmented CT slice (lung lobes shown in white), and (b) its corresponding Euclidean distance transform

3.1.3. Landmarking and Shape Model Generation

The atlas of each anatomical structure (i.e., lungs and the thoracic wall) is formed by extracting the zero level set of the binary images of each structure (Frangi et al, 2002). Let Θ_k and $\Im\Theta_k$ denote the shape in atlas-aligned coordinates and its signed Euclidean distance transform (Danielsson, 1980), respectively. The signed distance transform of an average shape can be obtained by computing $\Im\Theta_{average} = 1/n \sum_{k=1}^{n} \Im\Theta_k$. The average shape can be retrieved by thresholding the distance transform map to its zero-level set, as shown in figure 5. Next, this average shape is set as the temporary template and all other shapes are registered to this new shape using the registration procedure described in the previous section. This process is done iteratively until the error falls below a certain threshold.

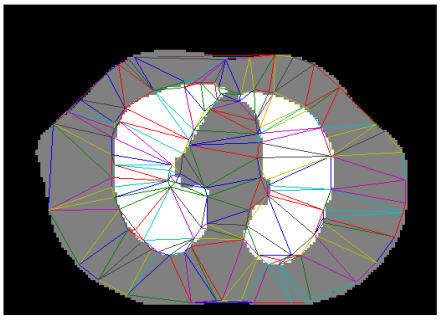

Figure 6: Extracting the lungs and the thoracic boundary.

Following the construction of the atlas, it needs to be landmarked. Ideally, a landmark is an anatomical point of interest that can be uniquely identified on a set of shapes. We consider the use of pseudo-landmarks, i.e., landmarks lying on the cross-sectional thorax boundary surface, which only define its geometric properties. Surface landmarks are considered, which correspond to vertices, resulting from the triangulation of the atlas binary volume. Having obtained good surface correspondences across the CT images in the dataset, PCA is applied on the data (i.e. vertices of the triangulation) treating the shapes of each CT as sampling points in the shape space (Lorenz and Krahnstöver, 2000). Given a set of examples of a shape x_i, we build a statistical shape model. Thus, by aligning *n* shape samples, consisting of *m* landmarks and applying principal component analysis on the sample distribution, any example *x* of the distribution can be expressed as a linear combination of eigenvectors *q*. The samples are composed of the 2D coordinates of the landmarks $x = (x_1, \dots, x_n, y_1, \dots, y_n)$, both on the chest wall and the lung lobes, with a one to one correspondence between the vector elements of a given index due to point correspondences. First, the mean shape vector $\bar{x}$ and the covariance matrix *C* that describes the correlation between vector elements are defined:

$$\bar{x} = 1/n \sum_{i=1}^{n} x_{i,} \tag{34}$$

$$C = \frac{1}{n-1} \sum_{i=1}^{n} (x_i - \bar{x}) \cdot (x_i - \bar{x})^T \tag{35}$$

Applying PCA on the covariance matrix *C* results in *3m* corresponding eigenvalues $\lambda_1 \geq \lambda_2 \geq \cdots \geq \lambda_{3m} \geq 0$ and *3m* eigenvectors q_k , $k = 1,2, \dots, 3m$. The eigenvector q_l corresponding to the largest eigenvalue λ_1 contains the largest portion of shape variations. If the number of training set vectors *n* is smaller than the shape vector dimension, the decomposition is simplified into finding *n* eigenvalues of the implicit covariance matrix $\tilde{C}$. The first *(n-1)* eigenvalues and eigenvectors of matrix *C* are determined as,

$$\lambda_i = \tilde{\lambda_i}\,;\; q_i = \frac{X \cdot \tilde{q_i}}{|X \cdot \tilde{q_i}|}\;, \qquad i = 1,2, \dots, (n-1), \tag{36}$$

where $\tilde{\lambda_i}$ are the eigenvalues and $\tilde{q_i}$ are the eigenvectors of the implicit covariance matrix $\tilde{C}$. By using these eigenvalues and eigenvectors, it is not only possible to reconstruct the original shape vectors, but also to generate new shape vectors (eigen shapes) $\acute{x_i}$,

$$\acute{x_i} = \bar{x} + w_i \cdot q_i \tag{37}$$

where w_i are weight vectors. By varying the shape parameters within the limits learnt from the training set, for instance, $|w_i| \leq \pm 3\sqrt{\lambda_i}$, we can generate shapes similar to those contained in the training set. The three dimensional space is spanned by the first three principal components, whose score units are normalized by the standard deviations of each mode. The vertices of the triangulation of the shape model serve as a rough universal thorax and lung contour model, as shown in figure 6. Once such a mesh model is built, it can be warped to conform to the shape of a new patient's thorax and superimposed to serve as the initial foreground area for the Kalman filtering. The anatomical shape information of the lungs and thorax helps speed up the Kalman filter by confining the search space of the Kalman filter to only the lung regions, thus improving its speed. Moreover, it enhances its accuracy by reducing outliers, penalizing regions that do not belong to the lungs.

3.1.5. Warping onto a new Patient Geometry

Obviously, a new patient will have a different boundary shape compared to the global shape model generated in the previous section. Thus, a warping step is necessary in order to superimpose the global shape model onto the new patient geometry efficiently. In order to achieve this, for any new thorax shape, we perform the following: We assume that the boundary information of the new patient is available via landmark points. A uniform spline interpolation is performed to obtain a continuous boundary, which is filled using morphological operators to obtain the thorax region displayed in white, as shown in figure 7(a). Next, the vertices of the global shape model are superimposed onto this thorax shape (red points in figure 7(a)) and the control points on the B-spline having minimum distance to the global shape vertices are selected as the new vertices to carry out the warping.

In order to warp the original global mesh vertices onto these new vertices coordinates, we parameterize the original global mesh onto these new vertices using the discrete harmonic map by (Eck et al, 1995). Common to almost all surface parameterization methods is the approximation of the underlying smooth surface *S* by a piecewise linear surface S_m, in the form of a *triangular mesh*, i.e., the union of a set $T = \{T_1, \ldots, T_q\}$ of triangles T_i such that the triangles intersect only at common vertices or edges. We will denote by *V* the set of vertices. If S_m has a boundary, then the boundary will be polygonal and we denote by V_b the set of vertices lying on the boundary and by V_I the set of interior vertices.

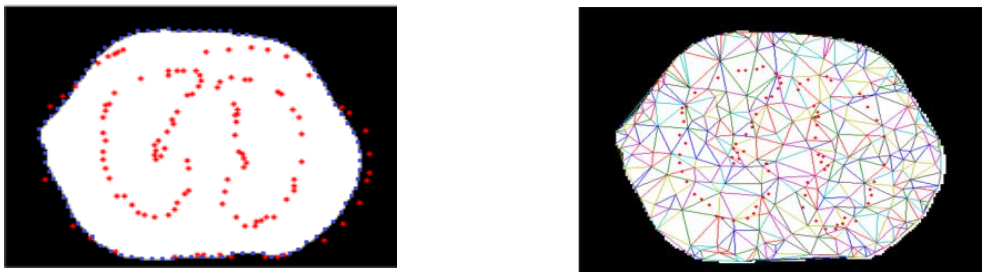

(a) (b)

Figure 7: Warping: (a) Superimposing the global lung shape (in red) onto the new patient's boundary, shown in white, (b) Final warped mesh onto new patient geomtery.

The most important parameterization task is to map a given disk-like surface $S \subset \mathcal{R}^3$ onto the plane. Working with a triangular mesh S_m, the goal is to find a suitable (polygonal) domain $S' \subset \mathcal{R}^3$ and a suitable piecewise linear mapping $\mathcal{F}$: $S_m \to S'$ that is linear on each triangle T_i in S_m and continuous (see figure 8).

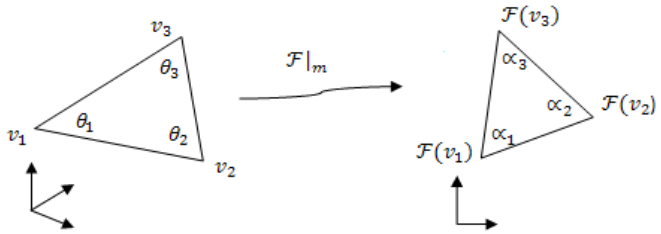

Figure 8: Atomic map between a mesh triangle and the corresponding parameter triangle.

Assuming S_m to be the original global mesh and ∂S_m its boundary and $\mathcal{F}_0$ the new vertices of the warped mesh, we first fix the boundary mapping, i.e., fix $\mathcal{F}|_{\partial S_m} = \mathcal{F}_0$, by mapping the polygonal boundary ∂S_m homeomorphically to the new vertices and we find a piecewise linear mapping which minimizes the Dirichlet energy,

$$E_D = \frac{1}{2}\int_{S_m} \left\| grad_{S_m} \mathcal{F} \right\|^2, \tag{38}$$

subject to the Dirichlet boundary condition $\mathcal{F}|_{\partial S_m} = \mathcal{F}_0$.

The main advantage of this method is that it is a quadratic minimization problem and reduces to solving a linear system of equations. The resulting new vertices are shown in figure 7(b), superimposed on the triangulation of the new patient's geometry. Finally, the left and right ROIs are selected by extracting the mesh elements, which fall inside the warped lung contours. These resulting regions are shown in figure 9.

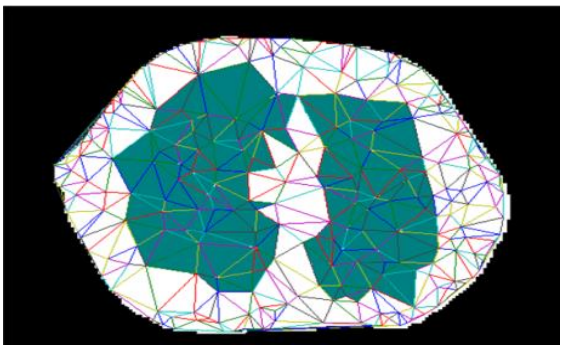

Figure 9: Extracting the lungs and the thoracic boundary.

3.2 Automatic Foreground Detector

Oncethe approximate location of the lungs (ROI_{left} and ROI_{right}) on the new patient is extracted, the initial contour to be used as the input to the Kalman filter is required. The proposed automatic method is as follows:

For each new reconstructed EIT image sequence (or mesh sequence to be accurate, as the segmentation is carried out over the meshes), $Vid = [I_1, I_2, \dots, I_M]$, where *M* is the number of images in the sequence,

a) Extract a 7s window (this ensures one full breathing cycle is included, see figure 10), and calculate the first images with the maximum and minimum absolute conductivity change values $\Delta\sigma$, inside in the left- and right-lung ROI regions. The resulting frames will correspond to the end expiration (I_{EE}) and end inspiration(I_{EI}) phases, respectively:

$$I_{EE} = find(\max[\text{abs}(area(ROI)_1, \dots, area(ROI)_7)])$$

$$I_{EI} = find(\min[\text{abs}(area(ROI)_1, \dots, area(ROI)_7)])$$

where ROI_1 denotes the ROI in the first second, etc.

b) Extract the centroids of the ROI_{left} and ROI_{right} regions in I_{EE} . For I_{EI}, calculate the absolute sum of conductivity change values in their respective ROIs and denote them by C_{Left} and C_{Right} (both real valued numbers). Steps (a) and (b) are shown in figure 10.

c) Find the boundary edges of the conductivity change regions by calculating the gradient of the mesh elements. First, we need to calculate the conductivity change gradient of ϕ at every vertex *v* of the unstructured lung mesh. In order to estimate the value of the gradient of ϕ at a vertex *v* of an element *E*, we use the method proposed in (Peyre and Cohen, 2006). Considering a 1-ring neighborhood (i.e., the immediate neighbors of any chosen vertex), given a local averaging function W, and a function f, the gradient operator G between two vertices *i* and *j*, is defined as,

$$\forall (i,j) \in E, i < j, \tag{39}$$

$$(Gf)_{i,j} = \sqrt{w_{ij}}(f_j - f_i) \in \mathcal{R}$$

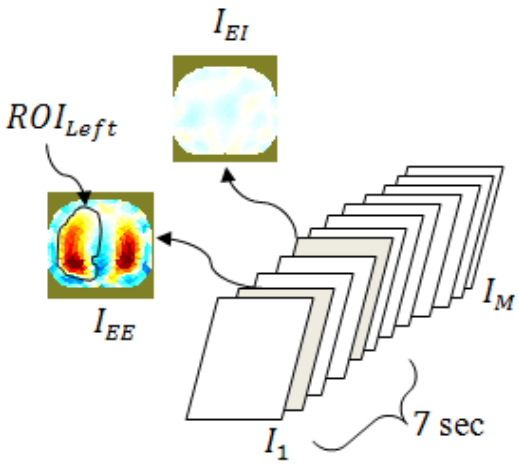

Figure 10: Schematic represenation of a sample video sequence.

For the local averaging, we use the square distances $w_{ij} = \|v_i - v_j\|^{-2}$, thus,

$$(Gf)_{i,j} = \frac{f(v_i) - f(v_j)}{\|v_i - v_j\|} \tag{40}$$

which is exactly the finite difference discretisation of a directional derivative.

d) For an image I_t at time $t < M$, we draw lines from the centroids of ROI_{left} and ROI_{right} at 20° intervals to cover a complete 360 cycle. This corresponds to 18 cuts through each ROI, and shown in figure 11(a) for an arbitrary angle θ.

e) For each angle θ, the mesh elements intersected by each line crosses are assembled (their total number denoted by *j)*, and arranged into a vector C_θ, containing the absolute gradient conductivity change values of that particular mesh element. For example, for the first element *E* from the centroid crossing the line at angle θ_1, having vertices *k*, *l* and *m*,

$$C_{E,1} = abs[(Gf)_{k,l} + (Gf)_{l,m} + (Gf)_{m,k}], \tag{41}$$
$$C_{\theta 1} = [C_{E,1}, C_{E,2}, \ldots, C_{E,j}]$$

This process is repeated for all directions and the resulting vectors are assembled into a cell array *Cfin*,

$$Cfin = [\, C_{\theta 1} \,,\, C_{\theta 2} \,, \ldots,\, C_{\theta R}] \tag{42}$$

where R is the total number of directions.

f) Next, in order to detect the foreground (i.e., conductivity change), we determine the element in each vector $C_{\theta i}\,, i = 1, \ldots, j$, of the cell array *Cfin*, which contains the maximum gradient conductivity change value that its nearest to the ROI boundary control point (e.g., point P_1 in figure 11(a)). This is performed for all directions. The boundary B_t, which represents the detected foreground at time *t* is extracted. The latter, is the convex hull of all the element vertices with the maximum gradient value in the ROI, $B_t = [(x_1, y_1), \ldots, (x_j, y_j)]$. Next, as in step (b) we calculate the absolute sum of conductivity change values in the current frame's ROIs (left and right), and denote them by $\acute{C}_{Left}$ and $\acute{C}_{Right}$.

g) Taking into account the fact of minimum conductivity change at EI,

While $(\acute{C}_{Left} + \acute{C}_{Right}) > (C_{Left} + C_{Right})$,use the extracted boundary points obtained in Step (f) as the new contour for the next frame at time *t+1* (i.e., $ROI_{t+1} = B_t$). The boundary points at each time instance are successively stored in a vector B_{vid} as,

$$B_{vid} = [{B_t}^T, {B_{t+1}}^T, \ldots, {B_M}^T]$$

Else $ROI_{t+1} = B_{M-(t+1)}$

The last statement ensures the contour expands again once it reaches a minimum area at end inspiration (EI), and prevents the contour from collapsing.

3.3 Segmentation using the Augmented Kalman Filter

Once the foreground contour representing the boundaries of the conductivity changes in each lobe has been extracted, the final position of the boundary points is the average of the Kalman filter output and the foreground detector. The segmentation scheme adopted is as follows:

- For the first image I_t in the image sequence, use the boundary B_t as the initial contour, with corresponding locations (x_t, y_t).
- Find the estimated new boundary positions at time t+1, denoted by B_{t+1}, comprised of the new postions $(\hat{x}_t, \hat{y}_t)$, using the Kalman filter.
- The final boundary coordinates are given by the average of the Kalman filter output and the foreground detector positions. For example, for a single point (x_t, y_t) on the boundary,

$$(x_{t+1},\, y_{t+1}) = \frac{1}{2}[(\hat{x}_t, \hat{y}_t) + (x_t, y_t)] \tag{43}$$

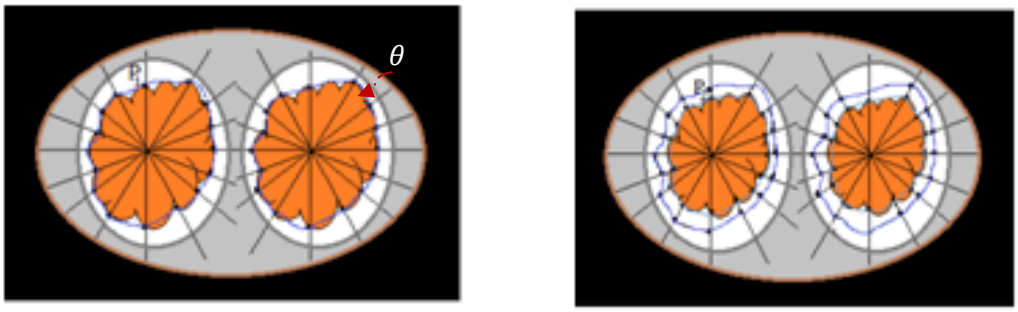

(a) (b)

Figure 11: Extracting the lungs and the thoracic boundary: (a) Original boundary at time t, (b) Boundary at time t+1.

4. Experimental results

4.1. Data Acquisition

Data were collected from a group of 10 male subjects with no known respiratory or cardiac abnormalities (age: mean 32; age range: 27-42). In each case, a 16 electrode adjacent protocol was chosen, and 16 electrodes were placed around the subject's lower thorax (4^{th}-6^{th} intercostal space on the mid-clavicular line). During the measurements, the subjects laid supine, and were asked to relax and breathe normally during a 3 min recording. A total of 2340 frames were recorded using a Sheffield mark 1 EIT system with a 50 kHz current drive (Brown, 2003). The measured voltage data were then imported into EIDORS (Adler and Lionheart, 2006) and the inverse problem was solved using the Gauss-Newton reconstruction algorithm on a 2D, 576-element thorax mesh model. A sample reconstruction is given in figure 12(a). The registration and FEM simulations were run under Matlab R2010a using an Intel Xeon 5130, 2.00 GHZ processor with 3.25GB of RAM.

4.2. Element Classification

The segmentation was carried out directly on the mesh, prior to any rasterization. Once an EIT image sequence was chosen, each of its elements was classified to foreground or lung lobe region according to the algorithm described in section 3. In order to use the Kalman filter for the conductivity change boundary tracking, we assume that the motion of the control points is merely translational along the oriented lines and is almost constant over the frames. For the experiments, the state space consists of the four parameters $(x, y, \dot{x}, \dot{y})$, with *(x,y)* representing the position of the points on the extracted boundaries and $(\dot{x}, \dot{y})$ representing their transition speed. The points move according to the dynamic matrix,

$$A = \begin{bmatrix} 1 & 0 & \sigma_t & 0 \\ 0 & 1 & 0 & \sigma_t \\ 0 & 0 & 1 & 0 \\ 0 & 0 & 0 & 1 \end{bmatrix}$$

where σ_t is the step size, which is assumed constant. The target measurements are given by,

$$C = \begin{bmatrix} 1 & 0 & 0 & 0 \\ 0 & 1 & 0 & 0 \end{bmatrix}$$

The exact position and speed at the beginning of measurements (output of foreground detector) is known, and thus the estimate covariance matrix *P* was set to zero. The gain of the measurement noise was set to 0.1. The step size σ_t was set to 0.1, and the matrix *H*, was set to a zero.

In frame t+1, the Kalman filter makes a prediction for a possible location of the object based on the contour of the output contour of the foreground detector. The final position is the average of the Kalman filter and the foreground detector position, as in (43). The process is then repeated on to the next frame, and so on. The resulting segmentation is shown in figure 12(c).

As previously mentioned, EIT images are particularly difficult to segment due to the fuzzy and ill-formed object boundaries in the reconstructions. Thus, a number of problems exist with the evaluation of segmentation algorithms for EIT image sequences. A critical issue is the lack of availability of ground truth data, due to which simulated EIT images are often employed to obtain a quantitative evaluation. Therefore, one cannot draw any definite conclusions about a particular algorithm since the simulated EIT images cannot accurately take into account all conditions (due to imaging as well as anatomical aspects) present during the acquisition of clinical data. Indeed, the usual method of expert validation, based on the estimation of the disparity with a manually delineated image (ground truth), suffers from human bias.

As can be seen in figure 12, both the proposed method and the method of (Zifan et al., 2011), produce reliable results. However, the efficiency of the proposed method relies on the fact that by using a global shape model of the lungs, no prior background modeling is required; this is in contrast to the method of (Zifan et al., 2011), which requires this. Moreover, another benefit of the proposed segmentation method is its fast segmentation average time of 4.31 seconds for an EI to EE, 2D EIT image sequence.

The proposed model was also compared to the Mixture of Gaussians (MoG) method described in (Stauffer and Grimson, 1999). The results of the proposed method in the EIT sequence of figure 12(a) are compared to the MoG method, and displayed in figure 13(c) for the same EIT sequence of figure 12 and for two other cases in figures 14 and 15. As it can be seen from these figures, the proposed method is able to detect better conductivity change regions, by exploiting the regional information of each element, as it evolves through time, thus recovering the correct shape change in the lobe regions. However, the method proposed by (Stauffer and Grimson, 1999) did not yield similar results. The main problems with this method are the presence of noise (small patches) in the foreground in some of the images and that the regions corresponding to the lungs appear to be over-segmented nearing end-expiration. This implies that the background model is matching the incorrect distribution for the background pixels.

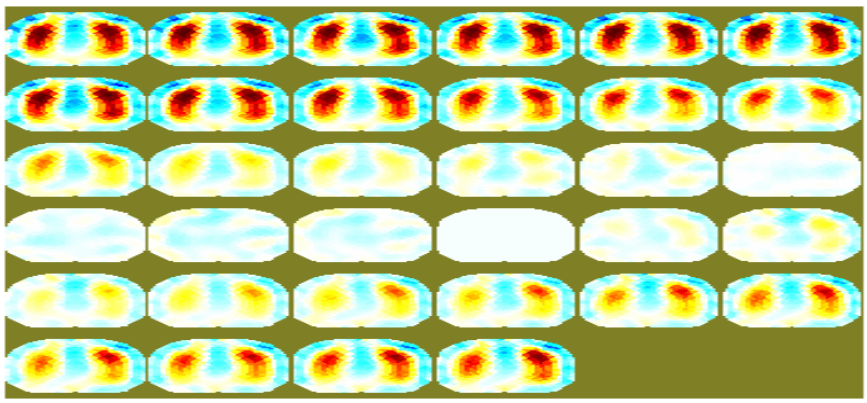

(a)

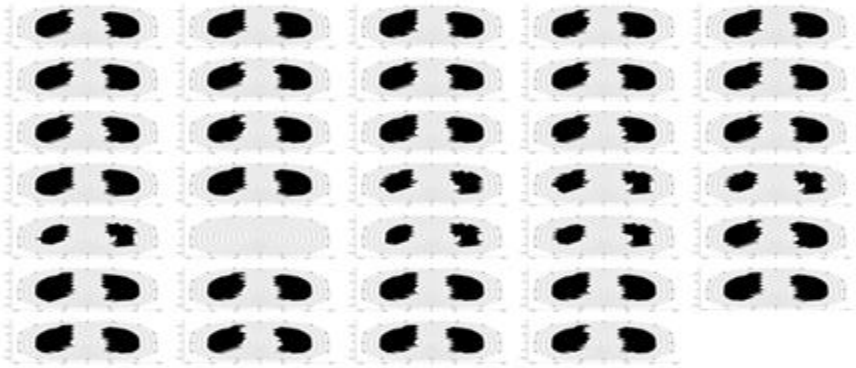

(b)

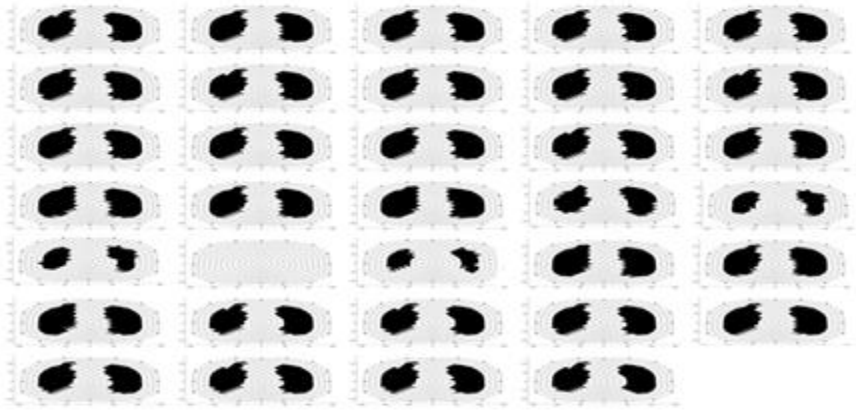

(c)

Figure 12: Segmentation results; image progression is from left to right, top to bottom. Full-breath cycle is shown: (a) Original image sequence, (b) Time-adaptive method described in (Zifan et al., 2011), (c) Proposed method.

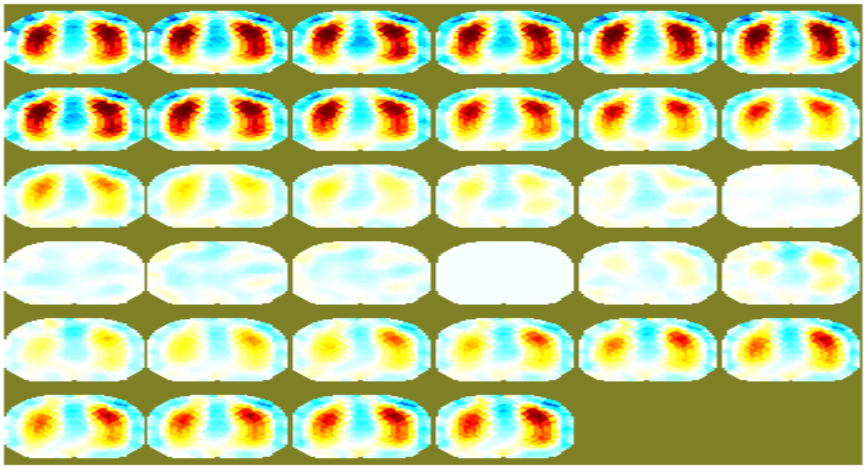

(a)

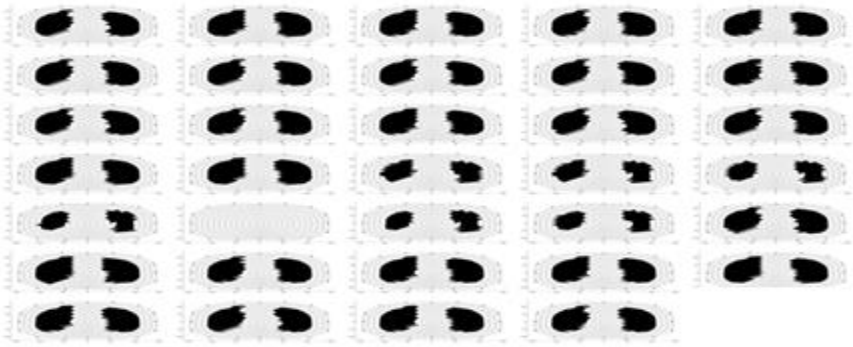

(b)

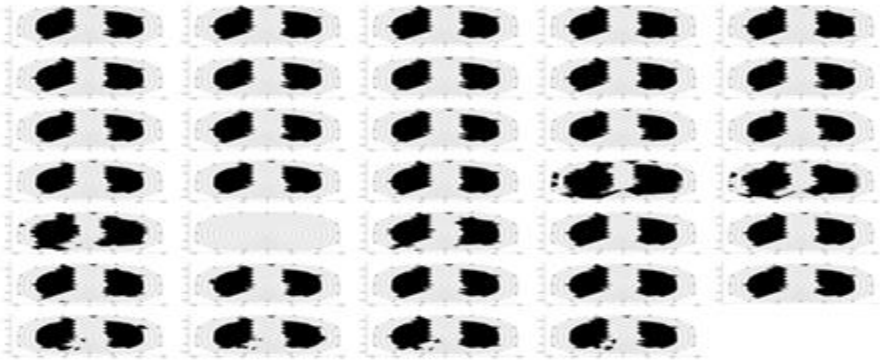

(c)

Figure 13: Segmentation results, image progression is from left to right, top to bottom. Full-breath cycle is shown: (a) Original image sequence, (b) Proposed method (c) Time-adaptive per-pixel MoG method.

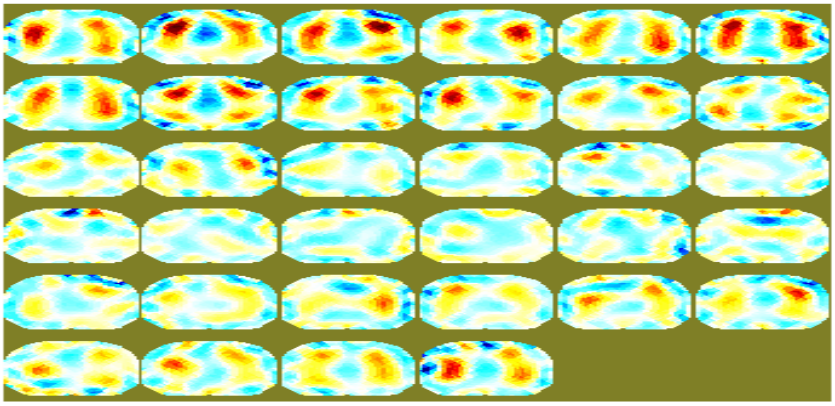

(a)

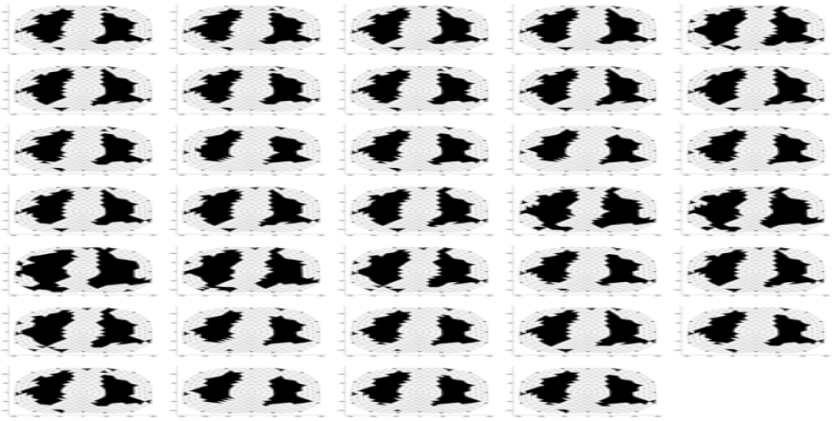

(b)

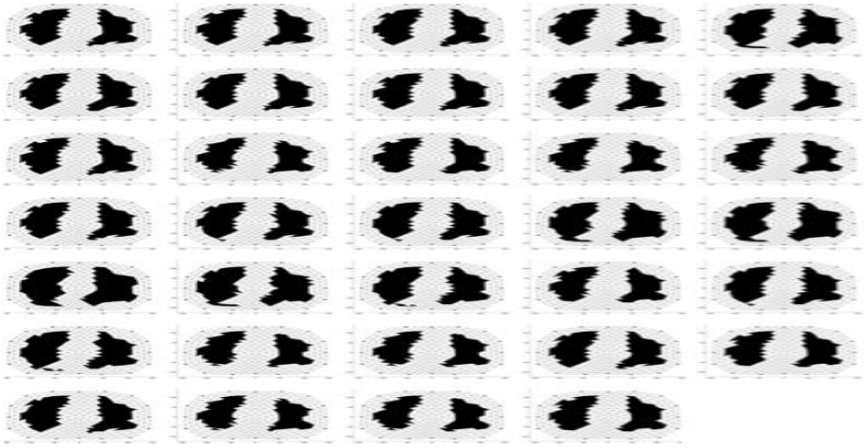

(c)

Figure 14: Segmentation results, image progression is from left to right, top to bottom. Full-breath cycle is shown: (a) Original image sequence, (c) Time-adaptive per-pixel MoG method, and (c) Proposed method.

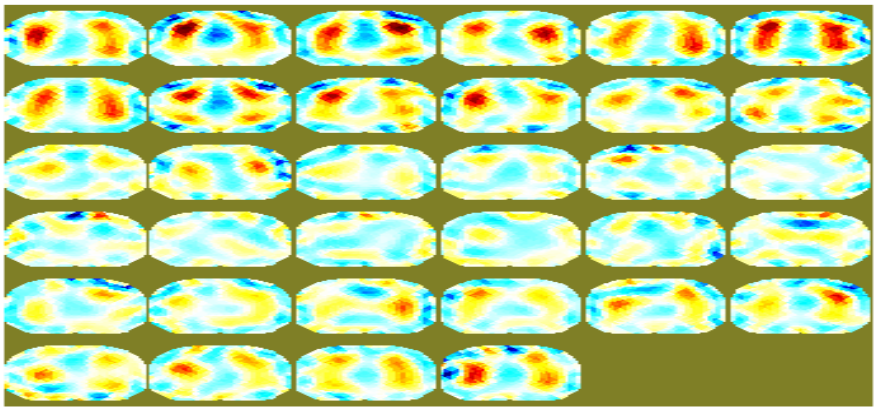

(a)

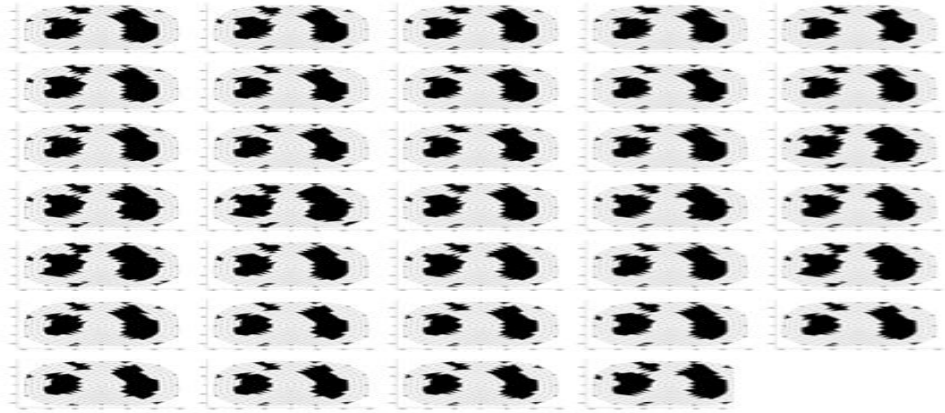

(b)

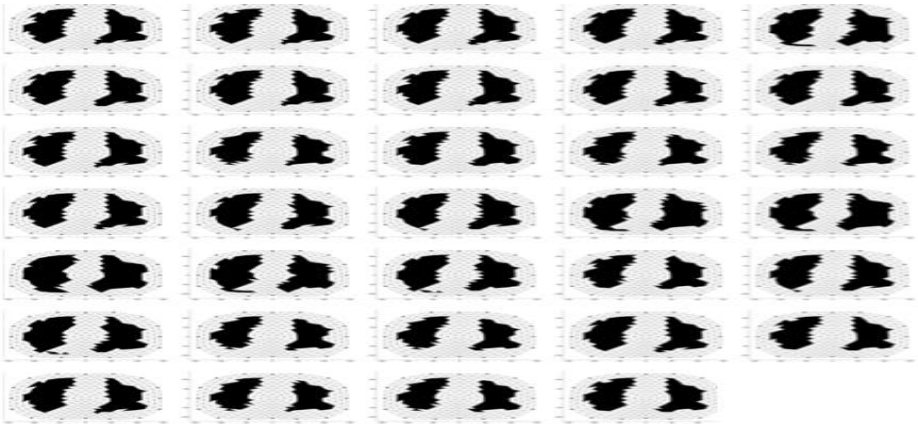

(c)

Figure 15: Segmentation results, image progression is from left to right, top to bottom. Full-breath cycle is shown: (a) Original image sequence, (c) Time-adaptive per-pixel MoG method, and (c) Proposed method.

Comparing the segmented ROIs obtained from the simulations with manual segmentations by three radiologists assessed the segmentation results. A mesh element is labeled as '1' if at least two out of the three radiologists assign it as a ground-truth element (i.e., element belongs to region of conductivity change). Area overlap (AO), false positive rate (FPR), false negative rate (FNR) are used as the performance metrics. The metrics are computed as follows (Park and Lee, 2009):

$$AO = 100 \times \frac{|S_1 \cap S_2|}{|S_1 \cup S_2|}$$

$$FPR = 100 \times \frac{|S_1 \cap {S_2}^c|}{|S_1 \cup S_2|} \tag{44}$$

$$FNR = 100 \times \frac{|{S_1}^c \cap S_2|}{|S_1 \cup S_2|}$$

where $S_1$are segmented regions and ${S_1}^c$ its complement. While, S_2 represents the ground truth data, delineated by the radiologists. FPR is used to quantify over-segmentation of conductivity change regions, while FNR contributes to under-segmentation within the segmented sequence.

Table 1: Performance evaluation comparison

(%)	AO	FPR	FNR
Proposed	97.089	2.177	0.734
Time-adaptive MOG	95.140	3.864	0.995
Time-adaptive	96.978	2.142	0.879

Table 1 shows the performance evaluation between the proposed fully automatic framework, with the time-adaptive MOG of (Stauffer and Grimson, 1999) and the adaptive method as described in (Zifan et al., 2011). The results show that the proposed method outperforms the two other methods, providing a high AO, while reducing false positives. The Time-adaptive method of (Zifan et al., 2011) shows comparable results to the proposed framework. However, the time-adaptive MOG lags the previous two methods, even though it gives a relatively high AO. The latter observation is mainly due to the existence of false positives, an over segmentation of the conductivity change regions. The former is not observed in the proposed method, as prior anatomical knowledge of lung lobes has been incorporated into the segmentation framework.

5. Conclusions

The work proposed in this contribution is a fast and robust segmentation pipeline for extracting conductivity changes in EIT lung images. The method involved a parallel approach, which combines the

outputs of a Kalman filter and an adaptive foreground detector to classify EIT mesh elements into lung and non-lung regions. Moreover, a prior model based on the anatomical position of the lungs in the thorax was generated in order to restrict the region of search and speed up computations. The results obtained from the different patient datasets show that this new approach can be successfully applied to robustly segment conductivity changes in EIT lung images. The proposed automatic segmentation framework operates directly on the resulting Finite Element meshes, prior to any rasterisation, thus reducing the propagation of errors in the reconstructed impedance change regions, due to interpolation. Application of the proposed method offers an alternative real-time automated framework to interactive segmentation commonly employed by EIT researchers and clinicians.

Acknowledgements

The authors gratefully acknowledge financial support for this research through Engineering and Physical Sciences Research Council (EPSRC) Grant EP/E029868/1 and the Dean of the School of Medicine, University of California, San Diego.

References

Adler A, Lionheart W R B 2006 Uses and abuses of EIDORS: An extensible software base for EIT *Physiol. Meas*. **27**:S25 {S42}

Anderson B D O, Moore J B 1979 Optimal Filtering. *New York: Prentice Hall Inc*. 129–133

Brown B H 2003 Electrical impedance tomography (EIT): a review *J Med Eng Technol*. **27** 97-108

Bucy R S, Joseph P D 2005 Filtering for Stochastic Processes with Applications to Guidance *John Wiley & Sons, 1968*; 2nd Edition, AMS Chelsea Publ.

Cachier P, Bardinet E 2003 Iconic feature based non-rigid registration: the PASHA algorithm, *Computer vision and Image understanding*, **89**:272-298

Cheng K S, Newell J C and Gisser D G 1989 Electrode models for electric current computed tomography *IEEE Trans. Biomed. Eng.* **36** 918–24

Dam E, Fletcher P, Pizer S 2008 Automatic shape model building based on principal geodesic analysis bootstrapping, *Medical Image Analysis*, **12**(2): 136-151

Daniel J, Withey, Zoltan J, and Kolesa 2008 A Review of medical image segmentation: Methods and available software *International Journal of Bioelectromagnetism*, **10**(3): 125-48

Danielsson P E 1980 Euclidean distance mapping Comp. *Graph. Imag. Process.* **14**: 227–248

Eck. M, DeRose T D, Duchamp T, Hoppe. H, Lounsbery M, Stuetzle W 1995 Multiresolution analysis of arbitrary meshes *Proceedings of SIGGRAPH '95* 173–182

ELCAP public lung image database,http://www.via.cornell.edu/databases/lungdb.html

Fleute L, Lavallee M S 1998 Building a complete surface model from sparse data using statistical shape models: Application to computer assisted knee surgery, *Medical Image Computing and Computer-Assisted Intervention-MICCAI 98*, 880–7

Frangi F, Rueckert D, Schnabel J A, Niessen W J 2002 Automatic construction of multiple-object three-dimensional statistical shape models: Application to cardiac modeling *IEEE-TMI* **21**:1151–66

Frerichs I, Hahm G, Schroder T, and Hellige G 1998 Electrical impedance tomography in monitoring experimental lung injury, *Intensive Care Med.* 24(8): 829-836

Frerichs I, Hahn G, Schiffmann H, et al 1999 Monitoring regional lung ventilation by functional electrical impedance tomography during assisted ventilation. Ann NY Acad Sci 873: 493–505.

Frerichs I 2000 Electrical impedance tomography (EIT) in applications related to lung and ventilation: a review of experimental and clinical activities *Physiological Measurement* **21** (2): R1

Frerichs I, Hinz J, Herrmann P, et al 2002 Detection of local lung air content by electrical impedance tomography compared with electron beam CT. *J Appl Physiol* 93: 660–666

Frerichs I, Pulletz S, Elke G, Reifferscheid F, Schadler D, Scholz J and Weiler N 2009 Assessment of changes in distribution of lung perfusion by electrical impedance tomography Respiration 77:282–91

Grychtol B, Wolf G K, Adler A and Arnold J H 2010 Towards lung EIT image segmentation: automatic classification of lung tissue state from analysis of EIT monitored recruitment maneuvers Physiol. Meas. 31:S31-S43

Hahn G, Frerichs I, Kleyer M, and Hellige G 1996 Local mechanics of the lung tissue determined by functional EIT *Physiol. Meas.* 17 (4A): A159-A166

Hendee W R and Russell R E 2002 Medical Imaging Physics, *4th* ed. Wiley-Liss, New York

Holder D S 1993 Clinical and Physiological Applications of EIT London *UCL Press*

Holder D S 2005 Electrical Impedance Tomography Methods, History and Applications Bristol, U.K.: Inst. Phys. Pub.

Hoerl A E 1962 Application of ridge analysis to regression problems Chemical Engineering Progress, **58**: 54-59

Hu S, Hoffman E A, Reinhardt J M M 2011 Automatic lung segmentation for accurate quantification of volumetric X–ray CT images *IEEE Transactions on Medical Imaging* **20** (6): 490–498

Ibanez L, Schroeder W NG L, Cates J 2005 The ITK Software Guide Kitware Inc.

Lorenz C, Krahnstöver N 2000 Generation of Point-Based 3D Statistical Shape Models for Anatomical Objects, *Computer Vision and Image Understanding* 177:175–91

Ma Z, Manuel J, Tavares R S, Natal Jorge R M, and Mascarenhas 2010 T A Review of Algorithms for Medical Image Segmentation and their Applications to the Female Pelvic Cavity *Computer Methods in Biomechanics and Biomedical Engineering*, **13**(2) 235-46

Modersitzki J 2004 Numerical methods for Image registration, Oxford University Press, New York.

Molinari M 2003 High Fidelity Imaging in Electrical Impedance Tomography, Ph.D. thesis, University of Southampton, Southampton, United Kingdom

Park J G, Lee C, 2009 Skull stripping based on region growing for magnetic resonance images *J Neuro Image* (47): 1394-1407

Pham D L, Xu C Y, Prince J L (2000) A survey of concurrent methods in medical image segmentation. Annu Rev Biom Eng, 2: 315-337

Pethig R 1984 Dielectric properties of biological materials: biophysical and medical applications *IEEE Trans. EI-19* **5**: 453-474

Peyre G, Cohen L D 2006 Geodesic Remeshing Using Front Propagation *Int. J. Comput. Vision* 6**9**(1): 145-156

Prasantha H S, Shashidhara H L, Murthy K N B, and Madhavi L G 2010 Medical image segmentation *International Journal on Computer Science and Engineering*, **2**(4): 1209-1218

Rajamani K, Styner M, Haydar T, Nolte L, Gonzalez Ballester M A 2007 Statistical deformable bone models for robust 3d surface extrapolation from sparse data, *Medical Image Analysis* **11**(2): 99-109

Rogeli P, Kovacic S 2006 Symmetric image registration, Medical image analysis **10**(3) 484-493

Singh K K, Singh A 2010 A Study of Image Segmentation Algorithms for Different Types of Images", *International Journal of Computer Science Issues*, **7**(5): 1694-0814

Stauffer M C, Grimson W 1999 Adaptive background mixture models for real-time tracking *IEEE*

Computer Society Conference on Computer Vision and Pattern Recognition (Cat. No PR00149)
Sorenson H W 1980 Parameter Estimation: Principles and Problems, Marcel Dekker
Subsol G, Thirion J, Ayache N 1998 A scheme for automatically building three-dimensional morphometric anatomical atlases: application to a skull atlas, *Medical Image Analysis* **2**(1): 37–60
Tychonoff A N, Arsenin V Y 1977 Solution of Ill-posed Problems *Washington: Winston & Sons*. ISBN 0-470-99124-0
Thirion J P 1995 Fast non-rigid matching of 3D medical images (Cedex: INRIA) http://hal.inria.fr/inria-00077268/en/
Victorino JA, Borges JB, Okamoto VN, et al (2004) Imbalances in regional lung ventilation: a validation study on electrical impedance tomography. Am J Respir Crit Care Med 169: 791–800
Wang H, Dong L 2005 Validation of an accelerated 'demons' algorithm for deformable image registration in radiation therapy, Physics in medicine and biology **50**(12) 2887-2905
Zhang Y J 2001 An Overview of Image and Video Segmentation in the last 40 years, *Proceedings of the 6th International Symposium on Signal Processing and Its Applications*, 144-151
Zifan A, Liatsis P, Kantartzis P, Canas R V 2011 Automatic Segmentation of Conductivity Changes in Electrical Impedance Tomography Images *Biosignals 2011* 215-221